Three-body fragmentation dynamics of the cyclopropane trication following 5.8-MeV/u Ni^{19+} impact

K. Z. Lin [1,2] D. L. Guo [2,3,*] X. L. Zhu [2,3] D. M. Zhao,[2,3] X. B. Zhu,[2,3] X. Shan [1,†]
S. F. Zhang,[2,3,‡] X. J. Chen [1] and X. Ma [2,3]

[1]*Department of Modern Physics, School of Physical Sciences, University of Science and Technology of China, Hefei 230026, China*
[2]*Institute of Modern Physics, Chinese Academy of Sciences, Lanzhou 730000, China*
[3]*School of Nuclear Science and Technology, University of Chinese Academy of Sciences, Beijing 100049, China*

The three-body fragmentation dynamics of cyclopropane (C_3H_6) induced by Ni^{19+} ions at an impact energy of 5.8 MeV/u are studied using a cold target recoil ion momentum spectroscopy (COLTRIMS) reaction microscope. Two completely measured three-body fragmentation channels of $C_3H_6^{3+}$ were identified definitely, i.e., $C_3H_6^{3+} \rightarrow H^+ + CH_2^+ + C_2H_3^+$ and $C_3H_6^{3+} \rightarrow H^+ + CH_3^+ + C_2H_2^+$. It is found that sequential fragmentation processes are dominant for the channels considered. For each channel, two distinct sequential mechanisms are distinguished, depending on whether the CH or CC bond breaks first. The observation is further supported by the characteristic kinetic energy release (KER) distributions associated with different mechanisms. Additionally, the reason for the prevalence of sequential fragmentation processes and their varying degrees of importance for the two channels are briefly discussed.

DOI: 10.1103/PhysRevA.109.022817

I. INTRODUCTION

The multibody fragmentation processes of molecules have been extensively studied both experimentally and theoretically for several decades. The interest in these processes stems not only from their fundamental aspects, but also from their importance in various applied fields such as planetary atmospheres, chemistry, plasma physics, and biology [1,2].

Different coincidence techniques have been developed in the past to study the fragmentation process. In particular, multiple-coincidence momentum imaging techniques such as the reaction microscope or cold target recoil ion momentum spectroscopy (COLTRIMS) [3–5] have been widely applied to measure the fragmentation process, enabling the reconstruction of the three-dimensional momentum vectors of all ionic fragments and thus determining the momentum correlations. Considerable effort has been devoted to studying the fragmentation dynamics of small molecules initiated by various ionizing radiation, such as charged ion [6–9], electron [10–15], intense laser field [16–18], or synchrotron radiation [19–21]. Different fragmentation mechanisms, such as sequential fragmentation in which the molecule dissociates by breaking chemical bonds one after another, and concerted breakup in which the chemical bonds break simultaneously [6,17,22–24], can be readily revealed from the momentum correlation among the final ionic fragments for three-body fragmentation processes. Additionally, the geometry of molecules can be reconstructed through direct multibody breakup using Coulomb-explosion imaging [25–28].

Among the various molecules investigated in the past, hydrocarbon molecules have gained special interest [29,30]. Hydrocarbons are widely present on Earth and in interstellar space and they play a crucial role in industry. In recent years, there has been significant attention towards the fragmentation of hydrocarbons induced by interacting with heavy ions, particularly due to its implications for radiation damage of biological tissues [31–33]. In the fragmentation process of hydrocarbon molecules, proton migration is a universal and important dynamic pattern. This is mainly because the mass of the hydrogen atom is much smaller compared to carbon. It has been demonstrated in a large number of studies that H migration was effectively involved in the fragmentation of the hydrocarbons. For example, it has been suggested that hydrocarbon fragmentation contributes significantly to the formation of the most prevalent interstellar molecular ion, H_3^+ [34–36], through proton migration. Proton migration may also be involved in H_2^+ formation during the fragmentation of the hydrocarbons [10,37,38]. Furthermore, proton migration-induced isomerization is also common in hydrocarbon molecules. For instance, Wei *et al*. [9] observed that the ethane dication $C_2H_6^{2+}$, in addition to direct Coulomb explosion, could undergo isomerization to intermediate $[H_2C(H_2)CH_2]^{2+}$ and further dissociate into $CH_3^+ + CH_3^+$.

Compared to chain-structure hydrocarbon molecules, the fragmentation of ring-structure hydrocarbon molecules is more interesting and complex as it involves ring-closing or ring-opening during fragmentation. Previous studies on ring-structure hydrocarbon molecules mainly focused on six-membered aromatic rings. For instance, studies on the

*guodalong@impcas.ac.cn
†xshan@ustc.edu.cn
‡zhangshf@impcas.ac.cn

ring-opening dynamics of 1,3-cyclohexadiene induced by photoexcitation have been conducted due to their relevance to critical reactions in biochemistry [39–42]. Recently, the ultrafast ring-opening fragmentation of benzene [43–45], followed by various hydrogen migrations [46], has also been investigated.

As the smallest naphthenes, cyclopropane is a fundamental structural element found in a broad range of naturally occurring and synthesized compounds [47]. Cyclopropane serves as an excellent prototype for studying ring deformation dynamics due to its unique molecular structure. It has a highly strained triangular carbon structure with D_{3h} symmetry in its ground state. The ionization potential of cyclopropane has been determined to be around 10 eV [48]. The ionization dynamics has been the subject of considerable discussion in the literature for many years. It has been found that the ionization process induces significant ring deformation and Jahn-Teller distortion [49,50]. Researchers have also investigated the ionization cross sections for electron [51] and bare-ion [52] impact ionization. It has been observed that the ionization cross sections for ion impact are weakly dependent on the projectile charge q compared with the q^2 dependence given by the first Born approximation [52]. Additionally, the isomer effects have attracted considerable interest for ionization of C_3H_6 isomers [52,53]. For ion impact ionization [52], the dominant product for cyclopropane is $C_3H_6^+$ ions, while for propene it is $C_3H_5^+$ ions, indicating an obvious isomer effect. However, no significant isomer effect was found for electron impact [53]. Electron impact experiments have also measured the electronic structure of cyclopropane [54] and the appearance potentials of ions formed from $C_3H_6^+$ [55].

Although previous studies have examined the fragmentation dynamics of cyclopropane, only a restricted range of scenarios have been explored. A joint experimental and theoretical study of dissociative double photoionization of $C_3H_6^{2+}$ revealed intensive ring-deformation and Jahn-Teller distortion by controlling the energies of photons [56]. More recently, a comparative study of the fragmentation dynamics of cyclopropane and propene following 4 keV/u Ar^{8+} collisions was reported [57]. The major two-body and three-body dissociation channels of $C_3H_6^{2+}$ dications were investigated, revealing obvious isomer effects. Despite these significant improvements, there is currently limited information available on the fragmentation dynamics of $C_3H_6^{3+}$ trication.

In the present work, the three-body fragmentation of cyclopropane induced by 5.8 MeV/u Ni^{19+} ion impact was studied by using a COLTRIMS spectrometer. While most previous experiments on ion-induced fragmentation of molecules focused on slow collisions, we chose a high energy for this study to explore the potential differences in fragmentation patterns compared to slow collisions since it is known that multiple-electron removal processes show strong dependence on the impact energy [58]. Interestingly, we observed the fragmentation of $C_3H_6^{3+}$, which is not seen in slow Ar^{8+} collisions. This observation was made possible by the multiple-electron removal ability of high-energy ions. The momentum vectors of all ionic fragments produced in the three-body fragmentation of $C_3H_6^{3+}$ were determined. The Dalitz plots and Newton diagrams revealing the momentum correlation of the fragments, as well as the kinetic energy release (KER) distributions, were

used to study the dissociation mechanisms of the three-body fragmentation dynamics. Our study provides valuable insights into the fragmentation dynamics of cyclic molecules induced by high-energy ion impact.

II. EXPERIMENTAL SETUP

The experiment was performed on a COLTRIMS setup newly installed at the Heavy Ion Research Facility in Lanzhou (HIRFL) of the Institute of Modern Physics, Chinese Academy of Science, Lanzhou, China. The new setup extends our investigations of ion-induced molecule fragmentation process to a much higher-energy region, from about 1 to 100 MeV/u. The details of the COLTRIMS have been given elsewhere [7,59]. Briefly, the Ni^{19+} ions produced in the electron cyclotron resonance (ECR) ion resource are extracted, charged selected by an analyzing magnet, accelerated by the sector focusing cyclotron (SFC) to the desired energy, and then transported to our experimental terminal. Several sets of quadrupole magnets and three sets of four-jaw adjustable slits upstream from the target chamber were used to focus and collimate the beam to a size of about 0.5 mm in diameter. In the reaction chamber, the Ni^{19+} ion beam crosses a two-stage differentially pumped supersonic gas jet beam produced by supersonic expansion of C_3H_6 gas through a 30-μm nozzle. The ion fragments and the electrons created in the collisions were extracted perpendicular to the incoming Ni^{19+} beam by a homogeneous electrostatic field and then traveled through a field-free drift tube. The acceleration region spans a distance of 107.5 mm, whereas the drift tube measures 215 mm in length. The ions and electrons were detected with multihit time and position-sensitive detectors located at the end of the drift tubes. In this work, the energy of Ni^{19+} ion beam is 5.8 MeV/u. The electrostatic field in the acceleration region is about 186 V/cm. The arriving time of the electron served as the reference for measuring the recoil ion time of flight (TOF).

The TOF information is used to identify the species of the ionic fragments. Different dissociation channels can be distinguished from the TOF correlation spectrum. The momentum vectors of the ionic fragments can be reconstructed using the time and position information recorded by the detector. By utilizing momentum conservation condition, the random coincidences can be efficiently suppressed.

For three-body dissociation processes, the Dalitz plot is a very powerful tool for investigating molecular fragmentation dynamics, as demonstrated in a large number of studies [60,61]. In the Dalitz plot, the Cartesian coordinates x and y are expressed as

$$x = \frac{\epsilon_1 - \epsilon_2}{\sqrt{3}}, \qquad (1)$$

$$y = \epsilon_3 - \frac{1}{3}, \qquad (2)$$

where the reduced kinetic energy $\epsilon_i = \vec{p}_i^2 / \Sigma_j \vec{p}_j^2$, with $\vec{p}_i^2$ and $\vec{p}_j^2$ being the momentum vectors of the ith and jth fragments. This definition implies that a set of three fragment momenta falls within a circle inscribed in an equilateral triangle, with each edge of the triangle representing a specific fragment. The reduced kinetic energy of a fragment can be determined by measuring its perpendicular distance to one of the three edges
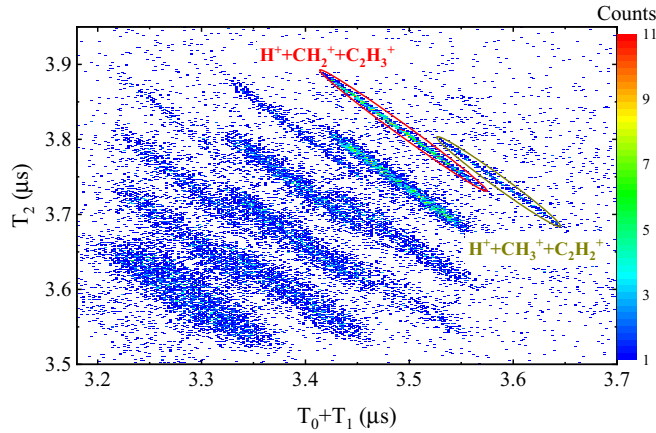
FIG. 1. Triple-ion TOF correlation map. The sum of the TOFs of the first and the second hit ions versus the TOF of the third hit ions. The solid ovals are used to select the events of the three-body dissociation channels.

FIG. 2. (a) Dalitz plot and (b) Newton diagram for the channel $C_3H_6^{3+} \rightarrow H^+ + CH_2^+ + C_2H_3^+$.

of the triangle. To gain further insights into the fragmentation dynamics, the Newton diagram is employed. In this diagram, the momentum of one of the three fragments is taken as 1.0 arbitrary unit, aligned along the x axis and represented by an arrow. The relative momentum vectors of the other two fragments with respect to the arrow are plotted in the upper and lower half planes of the diagram, respectively. The Newton diagram provides a straightforward visualization of the fragmentation dynamics [6].

III. RESULTS AND DISCUSSION

In the present experiment, the triple-ion TOF correlation map shown in Fig. 1 is employed to identify the different multibody dissociation channels. The x axis represents the sum of the TOFs of the first and second hit ions, while the y axis represents the TOF of the third hit ion. Various multibody dissociation channels could be identified in Fig. 1. The distinct sharp-line structures marked by solid ovals correspond to the three-body dissociation channels as follows:

$$C_3H_6^{3+} \rightarrow H^+ + CH_2^+ + C_2H_3^+, \tag{3}$$

$$C_3H_6^{3+} \rightarrow H^+ + CH_3^+ + C_2H_2^+. \tag{4}$$
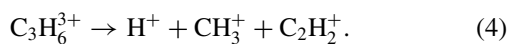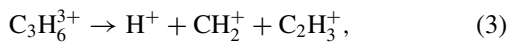
Apart from the above three-body dissociation channels, the structures located at the lower-left side of these channels are attributed to multibody fragmentation processes involving at least one undetected H (or H^+). We focus and discuss only the two fully measured three-body fragmentation channels of $C_3H_6^{3+}$ in the following analysis.

As depicted in Fig. 1, it is evident that the channel $C_3H_6^{3+} \rightarrow H^+ + CH_2^+ + C_2H_3^+$ is the preferred pathway for the three-body dissociation of $C_3H_6^{3+}$. Two oblique stripe structures marked by red and gray dashed rectangles are observed in the experimental Dalitz plot of this channel as shown in Fig. 2(a), implying that different fragmentation mechanisms may be involved in this channel. In Fig. 2(b), we present the Newton diagram normalized to the momentum of H^+ (represented by black arrow) for this channel. The two
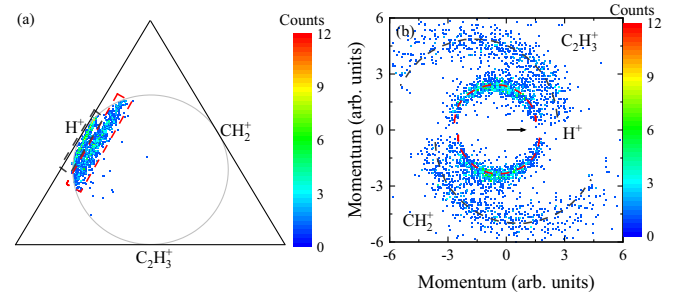
different contributions distinguished in the Dalitz plot can be identified as well in the Newton diagram. A clear circular structure marked by red dashed lines exhibits in the Newton diagram, which is an evidence of a sequential fragmentation process via $C_3H_6^{3+} \rightarrow H^+ + C_3H_5^{2+} \rightarrow H^+ + CH_2^+ + C_2H_3^+$, i.e., the initial CH bond cleavage is followed by subsequent CC bond cleavage. In addition, a weaker circular structure marked by the gray dashed semicircle appears in the Newton diagram, indicating a different sequential dissociation process occurring in this channel.

To further distinguish these two sequential process, the native frame method [62] is employed, which allows the determination of the relative contribution of different pathways. Assuming that the sequential process proceeds via $C_3H_6^{3+} \rightarrow H^+ + C_3H_5^{2+}$, Fig. 3(a) shows the native frame plot for this channel, where the angle θ, defined by the relative angle between the momentum vector of H^+ and $C_3H_5^{2+}$ in the native frame, is plotted versus the KER of $C_3H_5^{2+}$ in the second fragmentation step. It has been well established that in such a plot the sequential fragmentation exhibits a uniform distribution while the direct concerted fragmentation produces an inhomogeneous distribution with an intense area. Moreover, it would be possible to examine the validity of the assumption of the sequential process from the native frame plot: if the assumption is true, a vertical distribution appears, whereas an inclined distribution shows up. Thereby, the vertical distribution along the red dashed line shown in Fig. 3(a) corresponds to pathway I, i.e., $C_3H_6^{3+} \rightarrow H^+ + C_3H_5^{2+} \rightarrow H^+ + CH_2^+ + C_2H_3^+$. The corresponding Newton diagram is shown in Fig. 3(b). In contrast, the inclined distribution along the gray dashed line corresponds to another sequential fragmentation process denoted as pathway II. The Newton diagram of this pathway is shown in Fig. 3(c) where the momentum vector of CH_2^+ is fixed on the x axis and the relative momentum vectors of the H^+ ion and $C_2H_3^+$ ion are plotted on the lower and upper half planes, respectively. The appearance of a smaller circular structure in Fig. 3(c) indicates that pathway II corresponds to the sequential dissociation process $C_3H_6^{3+} \rightarrow CH_2^+ + C_2H_4^{2+} \rightarrow CH_2^+ + H^+ + C_2H_3^+$, where the initial CC bond breaking is followed by subsequent CH bond breaking.

The KER distributions are supportive of the assignment of the sequential pathways described above. Figure 3(d) displays the total KER distributions of channel $C_3H_6^{3+} \rightarrow H^+ + CH_2^+ + C_2H_3^+$. It can be seen that the total KER distribution of this channel exhibits a single peak centered at about 13.5 eV,
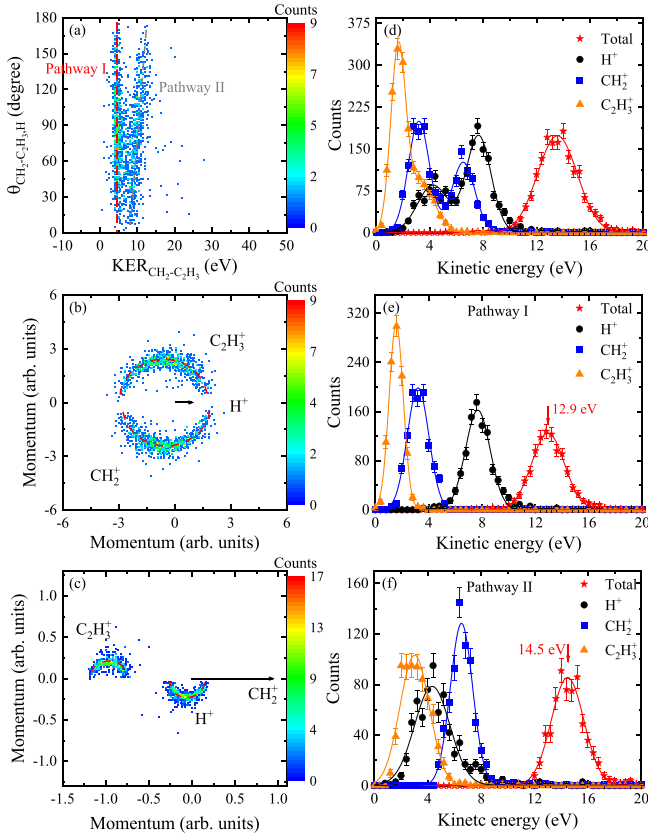
FIG. 3. (a) Native frame plot by assuming sequential fragmentation of $C_3H_6^{3+}$ via $H^+ + C_3H_5^{2+}$. [(b),(c)] Newton diagram for pathway I and pathway II, respectively. (d) KE distributions with all the experimental data for the channel $C_3H_6^{3+} \rightarrow H^+ + CH_2^+ + C_2H_3^+$. [(e),(f)] KE distributions for pathway I and pathway II, respectively.

FIG. 4. (a) Dalitz plot and (b) Newton diagram for the channel $C_3H_6^{3+} \rightarrow H^+ + CH_3^+ + C_2H_2^+$.

while there are two peaks presented in the kinetic energy (KE) distribution of the H^+ ion (4.6 eV and 7.8 eV) and CH_2^+ ion (3.5 eV and 6.6 eV). The $C_2H_3^+$ ion shows a peak centered around 1.8 eV with a shoulder structure at 3.2 eV. These distinct features correspond to the two sequential pathways. To gain further insight into the origin of these structures, the KE distributions of ionic fragments for the two pathways are illustrated in Figs. 3(e) and 3(f), respectively. Notably, the structures depicted in Fig. 3(d) arise from different KEs of the ionic fragments involved in different pathways.

By using Gaussian fittings, the average KER for pathway I and pathway II was determined to be 12.9 eV and 14.5 eV, respectively. The KE of the H^+ ion for pathway I is nearly twice as much as that for pathway II. The KE of the CH_2^+ ion for pathway I, in turn, is considerably lower compared to pathway II. The apparent difference of KEs can be readily attributed to the different Coulombic repulsions experienced by the H^+ ion in the two pathways. For pathway I, the majority of the KE of the H^+ ion originates from the first step, wherein it encounters a strong Coulombic repulsion caused by the double-charged intermediate $C_3H_5^{2+}$ ion. Unlike pathway I, the KE of the H^+ ion for pathway II primarily arises from the Coulombic repulsion between H^+ and $C_2H_3^+$ in the second step since $C_2H_3^+$ inherits most of the KE of the intermediate
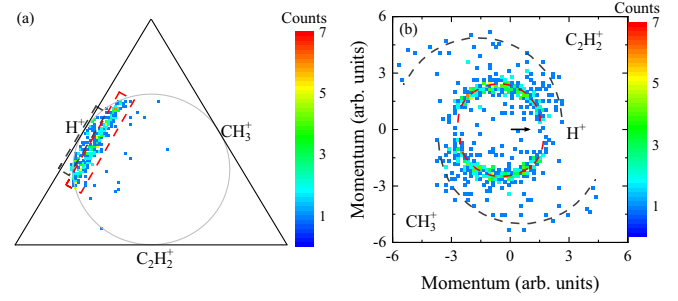
$C_2H_4^{2+}$ produced in the first step due to the small mass ratio between H^+ and $C_2H_3^+$. It thus follows that the KE of the H^+ ion for pathway II is roughly half that of pathway I, assuming the length of the broken CH bond is nearly equivalent for both pathways.

For channel $C_3H_6^{3+} \rightarrow H^+ + CH_3^+ + C_2H_2^+$ involving the proton migration, two oblique stripe structures marked by red and gray dashed rectangles are observed in the Dalitz plot shown in Fig. 4(a). The Newton plot in Fig. 4(b) also shows a prominent semicircular structure marked by a red dashed line and a weaker semicircular structure marked by a gray dashed line. This indicates that there are two distinct sequential fragmentation processes contributing to this pathway. The native frame plot is employed to further distinguish the two sequential processes, as shown in Fig. 5(a). Here it is assumed that the sequential process proceeds via $H^+ + C_3H_5^{2+}$. In the same way, the vertical distribution along the red dashed line and the inclined distribution along the gray dashed line correspond to two different sequential fragmentation processes (i.e., pathway I' and II') depending on which of the two kinds of bonds breaks first. In combination with the Newton diagram for the two contributions shown in Figs. 5(b) and 5(c), pathway I' is attributed to $C_3H_6^{3+} \rightarrow H^+ + C_3H_5^{2+} \rightarrow H^+ + CH_3^+ + C_2H_2^+$ while pathway II' corresponds to $C_3H_6^{3+} \rightarrow CH_3^+ + C_2H_3^{2+} \rightarrow CH_3^+ + H^+ + C_2H_2^+$.

Figure 5(d) shows the KE distributions of the ionic fragments. All three KE distributions exhibit a peak with a shoulder structure. The peak values for H^+, CH_3^+, and $C_2H_2^+$ ions are determined to be 7.4 eV, 2.7 eV, and 1.4 eV, respectively. The KE distributions for the two sequential pathways are presented in Figs. 5(e) and 5(f), respectively. It can be observed that the H^+ ion in pathway I' has much higher KE compared to pathway II', while the KE of CH_3^+ ion in pathway I' is considerably lower compared to pathway II'. This is expected as the H^+ ion experiences stronger Coulomb repulsion in pathway I', resulting in higher KE of H^+ due to its much smaller mass. Based on Gaussian fits, the average KER values for pathway I' and pathway II' are determined to be 12.8 eV and 14.0 eV, respectively.

To further investigate the sequential fragmentation dynamics, the KER distributions for each fragmentation step are reconstructed [7,62] and compared with previous studies. In Ref. [63], Głuch *et al.* studied the fragmentation of $C_3H_5^{2+} \rightarrow CH_3^+ + C_2H_2^+$ and the KER value is determined to be 4.58 eV. Based on *ab initio* quantum-chemical calculations, they re-

FIG. 5. (a) Native frame plot by assuming sequential fragmentation of $C_3H_6^{3+}$ via $H^+ + C_3H_5^{2+}$. [(b),(c)] Newton diagram for pathway I′ and pathway II′, respectively. (d) KE distributions with all the experimental data for the channel $C_3H_6^{3+} \rightarrow H^+ + CH_3^+ + C_2H_2^+$. [(e),(f)] KE distributions for pathway I′ and pathway II′, respectively.

TABLE I. The relative branching ratios of the two sequential pathways for the two dissociation channels.

Channel	Relative branching ratio	
	Pathway I (I′)	Pathway II (II′)
$H^+ + CH_2^+ + C_2H_3^+$	$58.8\% \pm 2.0\%$	$41.2\% \pm 1.4\%$
$H^+ + CH_3^+ + C_2H_2^+$	$81.7\% \pm 5.8\%$	$18.3\% \pm 1.3\%$

explain the presence of $C_3H_5^{2+}$ in the TOF spectrum. In this case, the lifetime of the $C_3H_5^{2+}$ ion formed from $C_3H_6^{2+}$ should be long enough to reach the ion detector. On the other hand, the observation of a complete semicircle structure in Newton diagrams and the absence of ion pair $H^+ + C_3H_5^{2+}$ island in ion-ion coincidence TOF map imply that the lifetime of the intermediate $C_3H_5^{2+}$ ion formed from $C_3H_6^{3+}$ is comparable to its own rotation period of no more than a few ps, which is much shorter than that of the $C_3H_5^{2+}$ formed from $C_3H_6^{2+}$. The intermediate state of the $C_3H_5^{2+}$ ion formed via emission of a H^+ by $C_3H_6^{3+}$ can survive for some time and then further dissociate into two C-based ions.

We now turn to a comparison of the two channels. The relative contributions from the respective two sequential pathways demonstrate varying degrees of importance. Table I displays the relative branching ratios of the two sequential pathways for the two dissociation channels. Different from the channel $H^+ + CH_2^+ + C_2H_3^+$, where the contributions of the two sequential pathways are comparable, for the channel $H^+ + CH_3^+ + C_2H_2^+$ which involves proton migration, the contribution of pathway I′ is much larger than pathway II′. This can be understood considering the timescales of the relevant processes. The estimated timescale for the first step of sequential fragmentation is typically around tens of fs [64,65], whereas the timescale for proton migration is on the order of tens to 100 fs [66,67]. Clearly, the timescale of the first step of sequential fragmentation is comparable to that of proton migration, indicating that proton migration may compete with the first fragmentation step for the channel involving proton migration. Depending on in which step proton migration occurs, the relative contributions of the different sequential processes may vary significantly. For the channel $C_3H_6^{3+} \rightarrow H^+ + CH_3^+ + C_2H_2^+$, pathway I′ could be dominant assuming that the first step of sequential fragmentation is faster than proton migration.

Finally, it should be noted that the experiment was conducted using highly charged (Ni^{19+}) ions at an impact energy of 5.8 MeV/u, which is in a largely unexplored energy range. Unlike previous studies on molecule fragmentation primarily performed using low- and intermediate-energy ions [6,68–72], where concerted breakup plays a vital role, the sequential fragmentation pathways dominate in the present experiment at the much higher energy considered for both dissociation channels. It is plausible to surmise that the velocity of projectiles has a strong influence on the dynamics of molecular fragmentation. This hypothesis is supported by previous studies using different projectile velocities, which indicated that multiple-electron removal processes exhibit a strong dependence on the impact energy [5,58]. For instance, in the high-energy

vealed the fragmentation mechanism, i.e., the $C_3H_5^{2+}$ with the doublet C_s symmetry dissociates into CH_3^+ (singlet, D_{3h} symmetry) and vinylidene $C_2H_2^+$ (doublet, C_{2v} symmetry) via a transition state. In the present work, the KER for the second fragmentation step in pathway I′ is approximately 4.7 eV, as can be seen in Fig. 5(a), which closely matches the reported KER value by Głuch *et al*. [63], indicating that the proposed dissociation mechanism may explain the second fragmentation step in pathway I′.

According to the analysis above, it is evident that the sequential fragmentation pathways mediated by $C_3H_5^{2+}$ play a significant role in the channels $C_3H_6^{3+} \rightarrow H^+ + CH_2^+ + C_2H_3^+$ and $C_3H_6^{3+} \rightarrow H^+ + CH_3^+ + C_2H_2^+$. Interestingly, no ion pairs of $H^+ + C_3H_5^{2+}$ were found in the present ion-ion coincidence TOF map, while a peak corresponding to $C_3H_5^{2+}$ ion were indeed observed in the TOF spectrum of the first hit ion, consistent with the observations of dissociative double ionization of C_3H_6 [56] and the fragmentation of C_3H_6 following 4 keV/u Ar^{8+} collisions [57]. We speculate that the electronic states of the $C_3H_5^{2+}$ ions formed from $C_3H_6^{2+}$ and $C_3H_6^{3+}$ may be quite different, leading to a large difference in lifetimes of $C_3H_5^{2+}$ ions. On the one hand, the proposed mechanism of single neutral hydrogen evaporation in [56] may

region, postcollisional ionization mechanisms such as Auger and Coster-Krönig dominate, whereas at low and intermediate energies, direct multiple ionization of the outer shell of the target is the main contribution [73]. The fragmentation patterns can be influenced by the distribution of primary vacancies resulting from the different mechanisms of electron removal [68]. However, it is worthwhile to note that, for the fragmentation of benzene [44,46], which possesses a ring structure, only the sequential mechanisms are observed, in contrast to small molecules where concerted breakup is the dominant fragmentation mechanism [12,17,62]. This suggests that the molecular structure itself may serve as an alternative explanation for the observations. Therefore, further theoretical investigations beyond qualitative explanations, as well as extensive experimental measurements, are essential to provide a more refined analysis.

IV. SUMMARY

In summary, the three-body fragmentation dynamics of C_3H_6 induced by the 5.8 MeV/u Ni^{19+} ion beam were investigated using a COLTRIMS setup. The fragmentation dynamics were revealed for the two most abundant three-body dissociation channels of $C_3H_6^{3+}$, i.e., $C_3H_6^{3+} \rightarrow H^+ + CH_2^+ + C_2H_3^+$ and $C_3H_6^{3+} \rightarrow H^+ + CH_3^+ + C_2H_2^+$, using Dalitz plots, Newton diagrams, and the native frame method. It was discovered that both channels primarily proceed through sequential frag-

mentation processes, with two distinct sequential mechanisms identified for each channel depending on which type of bond, CH or CC, breaks first. The KER distributions of the two channels were also obtained. For different pathways, the difference of the kinetic energy of a specific fragment is distinct between different pathways, which is understandable and supportive of the fragmentation dynamics. Additionally, the KER distribution of each breakup in the channel $C_3H_6^{3+} \rightarrow H^+ + CH_3^+ + C_2H_2^+$ was reconstructed and compared with available studies, offering new insights into the fragmentation dynamics. Furthermore, we briefly discussed the prevalence of sequential fragmentation processes and the varying degrees of their importance for the two channels, as well as the absence of intermediate ion pairs.

[1] E. Alizadeh, T. M. Orlando, and L. Sanche, Annu. Rev. Phys. Chem. **66**, 379 (2015).

[2] K. Bartschat and M. J. Kushner, Proc. Natl. Acad. Sci. USA **113**, 7026 (2016).

[3] C. Cocke and R. Olson, Phys. Rep. **205**, 153 (1991).

[4] R. Dörner, V. Mergel, O. Jagutzki, L. Spielberger, J. Ullrich, R. Moshammer, and H. Schmidt-Böcking, Phys. Rep. **330**, 95 (2000).

[5] J. Ullrich, R. Moshammer, A. Dorn, R. Dörner, L. P. H. Schmidt, and H. Schmidt-Böcking, Rep. Prog. Phys. **66**, 1463 (2003).

[6] N. Neumann, D. Hant, L. P. H. Schmidt, J. Titze, T. Jahnke, A. Czasch, M. S. Schöffler, K. Kreidi, O. Jagutzki, H. Schmidt-Böcking, and R. Dörner, Phys. Rev. Lett. **104**, 103201 (2010).

[7] S. Yan, X. L. Zhu, P. Zhang, X. Ma, W. T. Feng, Y. Gao, S. Xu, Q. S. Zhao, S. F. Zhang, D. L. Guo, D. M. Zhao, R. T. Zhang, Z. K. Huang, H. B. Wang, and X. J. Zhang, Phys. Rev. A **94**, 032708 (2016).

[8] X. Zhu, X. Hu, S. Yan, Y. Peng, W. Feng, D. Guo, Y. Gao, S. Zhang, A. Cassimi, J. Xu, D. Zhao, D. Dong, B. Hai, Y. Wu, J. Wang, and X. Ma, Nat. Commun. **11**, 2987 (2020).

[9] L. Wei, C.-S. Lam, Y. Zhang, B. Ren, J. Han, B. Wang, Y. Zou, L. Chen, K.-C. Lau, and B. Wei, J. Phys. Chem. Lett. **12**, 5789 (2021).

[10] R. Flammini, M. Satta, E. Fainelli, G. Alberti, F. Maracci, and L. Avaldi, New J. Phys. **11**, 083006 (2009).

[11] X. Ren, T. Pflüger, M. Weyland, W. Y. Baek, H. Rabus, J. Ullrich, and A. Dorn, J. Chem. Phys. **141**, 134314 (2014).

[12] E. Wang, X. Shan, Z. Shen, M. Gong, Y. Tang, Y. Pan, K.-C. Lau, and X. Chen, Phys. Rev. A **91**, 052711 (2015).

[13] E. Wang, M. Gong, Z. Shen, X. Shan, X. Ren, A. Dorn, and X. Chen, J. Chem. Phys. **149**, 204301 (2018).

[14] L. Chen, X. Shan, E. Wang, X. Ren, X. Zhao, W. Huang, and X. Chen, Phys. Rev. A **100**, 062707 (2019).

[15] L. Chen, E. Wang, X. Shan, Z. Shen, X. Zhao, and X. Chen, Phys. Rev. A **104**, 032814 (2021).

[16] J. H. Posthumus, Rep. Prog. Phys. **67**, 623 (2004).

[17] C. Wu, C. Wu, D. Song, H. Su, Y. Yang, Z. Wu, X. Liu, H. Liu, M. Li, Y. Deng, Y. Liu, L.-Y. Peng, H. Jiang, and Q. Gong, Phys. Rev. Lett. **110**, 103601 (2013).

[18] K. Lin, X. Hu, S. Pan, F. Chen, Q. Ji, W. Zhang, H. Li, J. Qiang, F. Sun, X. Gong, H. Li, P. Lu, J. Wang, Y. Wu, and J. Wu, J. Phys. Chem. Lett. **11**, 3129 (2020).

[19] J. B. Williams, C. S. Trevisan, M. S. Schöffler, T. Jahnke, I. Bocharova, H. Kim, B. Ulrich, R. Wallauer, F. Sturm, T. N. Rescigno, A. Belkacem, R. Dörner, T. Weber, C. W. McCurdy, and A. L. Landers, Phys. Rev. Lett. **108**, 233002 (2012).

[20] J. H. D. Eland, L. Andric, P. Linusson, L. Hedin, S. Plogmaker, J. Palaudoux, F. Penent, P. Lablanquie, and R. Feifel, J. Chem. Phys. **135**, 134309 (2011).

[21] A. Ramadhan, B. Wales, R. Karimi, I. Gauthier, M. MacDonald, L. Zuin, and J. Sanderson, J. Phys. B: At., Mol. Opt. Phys. **49**, 215602 (2016).

[22] C.-M. Tseng, M. Fushitani, A. Matsuda, and A. Hishikawa, J. Electron Spectrosc. Relat. Phenom. **228**, 25 (2018).

[23] X. Yu, X. Zhao, Z. Wang, Y. Yang, X. Zhang, P. Ma, X. Li, C. Wang, X. Xu, C. Wang, D. Zhang, S. Luo, and D. Ding, Phys. Rev. A **104**, 053104 (2021).

[24] X. Yu, X. Zhang, X. Hu, X. Zhao, D. Ren, X. Li, P. Ma, C. Wang, Y. Wu, S. Luo, and D. Ding, Phys. Rev. Lett. **129**, 023001 (2022).

[25] M. Pitzer, M. Kunitski, A. S. Johnson, T. Jahnke, H. Sann, F. Sturm, L. P. H. Schmidt, H. Schmidt-Böcking, R. Dörner, J. Stohner, J. Kiedrowski, M. Reggelin, S. Marquardt, A. Schießer, R. Berger, and M. S. Schöffler, Science **341**, 1096 (2013).

[26] M. Pitzer, G. Kastirke, M. Kunitski, T. Jahnke, T. Bauer, C. Goihl, F. Trinter, C. Schober, K. Henrichs, J. Becht, S. Zeller, H. Gassert, M. Waitz, A. Kuhlins, H. Sann, F. Sturm, F. Wiegandt, R. Wallauer, L. P. H. Schmidt, A. S. Johnson *et al.*, ChemPhysChem **17**, 2465 (2016).

[27] S. Bhattacharyya, K. Borne, F. Ziaee, S. Pathak, E. Wang, A. S. Venkatachalam, X. Li, N. Marshall, K. D. Carnes, C. W. Fehrenbach, T. Severt, I. Ben-Itzhak, A. Rudenko, and D. Rolles, J. Phys. Chem. Lett. **13**, 5845 (2022).

[28] X. Li, A. Rudenko, M. S. Schöffler, N. Anders, T. M. Baumann, S. Eckart, B. Erk, A. De Fanis, K. Fehre, R. Dörner, L. Foucar, S. Grundmann, P. Grychtol, A. Hartung, M. Hofmann, M. Ilchen, C. Janke, G. Kastirke, M. Kircher, K. Kubicek *et al.*, Phys. Rev. Res. **4**, 013029 (2022).

[29] M. R. Swain, G. Vasisht, and G. Tinetti, Nature (London) **452**, 329 (2008).

[30] J. Roithová and D. Schröder, Phys. Chem. Chem. Phys. **9**, 731 (2007).

[31] Z. Deng, I. Bald, E. Illenberger, and M. A. Huels, Phys. Rev. Lett. **96**, 243203 (2006).

[32] M. Capron, S. Díaz-Tendero, S. Maclot, A. Domaracka, E. Lattouf, A. Ławicki, R. Maisonny, J.-Y. Chesnel, A. Méry, J.-C. Poully, J. Rangama, L. Adoui, F. Martín, M. Alcamí, P. Rousseau, and B. A. Huber, Chem. Eur. J. **18**, 9321 (2012).

[33] P. López-Tarifa, M.-A. Hervé du Penhoat, R. Vuilleumier, M.-P. Gaigeot, I. Tavernelli, A. Le Padellec, J.-P. Champeaux, M. Alcamí, P. Moretto-Capelle, F. Martín, and M.-F. Politis, Phys. Rev. Lett. **107**, 023202 (2011).

[34] N. Ekanayake, M. Nairat, B. Kaderiya, P. Feizollah, B. Jochim, T. Severt, B. Berry, K. R. Pandiri, K. D. Carnes, S. Pathak, D. Rolles, A. Rudenko, I. Ben-Itzhak, C. A. Mancuso, B. S. Fales, J. E. Jackson, B. G. Levine, and M. Dantus, Nat. Coummun. **7**, 4703 (2017).

[35] E. Wang, X. Ren, and A. Dorn, Phys. Rev. Lett. **126**, 103402 (2021).

[36] K. Gope, E. Livshits, D. M. Bittner, R. Baer, and D. Strasser, J. Phys. Chem. Lett. **11**, 8108 (2020).

[37] D. L. Hansen, J. Cotter, G. R. Fisher, K. T. Leung, R. Martin, P. Neill, R. C. C. Perera, M. Simon, Y. Uehara, B. Vanderford, S. B. Whitfield, and D. W. Lindle, J. Phys. B: At., Mol. Opt. Phys. **32**, 2629 (1999).

[38] Y. Zhang, B. Wang, L. Wei, T. Jiang, W. Yu, R. Hutton, Y. Zou, L. Chen, and B. Wei, J. Chem. Phys. **150**, 204303 (2019).

[39] A. R. Attar, A. Bhattacherjee, C. D. Pemmaraju, K. Schnorr, K. D. Closser, D. Prendergast, and S. R. Leone, Science **356**, 54 (2017).

[40] T. J. A. Wolf, D. M. Sanchez, J. Yang, R. M. Parrish, J. P. F. Nunes, M. Centurion, R. Coffee, J. P. Cryan, M. Gühr, K. Hegazy *et al.*, Nat. Chem. **11**, 504 (2019).

[41] S. Adachi, M. Sato, and T. Suzuki, J. Phys. Chem. Lett. **6**, 343 (2015).

[42] M. Tudorovskaya, R. S. Minns, and A. Kirrander, Phys. Chem. Chem. Phys. **20**, 17714 (2018).

[43] T. Zyubina, G.-S. Kim, A. Mebel, A. S. Lin, and A. Bandrauk, Chem. Phys. Lett. **359**, 253 (2002).

[44] A. Matsuda, M. Fushitani, R. D. Thomas, V. Zhaunerchyk, and A. Hishikawa, J. Phys. Chem. A **113**, 2254 (2009).

[45] X. Yu, Y. Liu, K. Deng, X. Zhang, P. Ma, X. Li, C. Wang, Z. Cui, S. Luo, and D. Ding, Phys. Rev. A **105**, 063105 (2022).

[46] J. Zhou, Y. Li, Y. Wang, S. Jia, X. Xue, T. Yang, Z. Zhang, A. Dorn, and X. Ren, Phys. Rev. A **104**, 032807 (2021).

[47] H. Lebel, J.-F. Marcoux, C. Molinaro, and A. B. Charette, Chem. Rev. **103**, 977 (2003).

[48] F. H. Field and E. A. Hinkle, J. Chem. Phys. **18**, 1122 (1950).

[49] R. J. Buenker and S. D. Peyerimhoff, J. Phys. Chem. **73**, 1299 (1969).

[50] H. Basch, M. B. Robin, N. A. Kuebler, C. Baker, and D. W. Turner, J. Chem. Phys. **51**, 52 (1969).

[51] H. Nishimura and H. Tawara, J. Phys. B: At. Mol. Opt. Phys. **27**, 2063 (1994).

[52] T. Nakazato, T. Matsuo, T. Kohno, Y. Ohno, S. Watanabe, and T. Murakami, J. Phys.: Conf. Ser. **163**, 012063 (2009).

[53] H. Deutsch, K. Becker, R. K. Janev, M. Probst, and T. D. Märk, J. Phys. B: At. Mol. Opt. Phys. **33**, L865 (2000).

[54] P. Rademacher, ChemPhysChem **4**, 1237 (2003).

[55] F. H. Field, J. Chem. Phys. **20**, 1734 (1952).

[56] S. Oghbaie, M. Gisselbrecht, E. P. Månsson, J. Laksman, C. Stråhlman, A. Sankari, and S. L. Sorensen, Phys. Chem. Chem. Phys. **19**, 19631 (2017).

[57] D. L. Guo, K. Z. Lin, X. L. Zhu, R. T. Zhang, Y. Gao, D. M. Zhao, X. B. Zhu, S. F. Zhang, and X. Ma, J. Chem. Phys. **157**, 154309 (2022).

[58] A. C. Tavares, C. C. Montanari, J. E. Miraglia, and G. Sigaud, J. Phys. B: At. Mol. Opt. Phys. **47**, 045201 (2014).

[59] X. Ma, R. T. Zhang, S. F. Zhang, X. L. Zhu, W. T. Feng, D. L. Guo, B. Li, H. P. Liu, C. Y. Li, J. G. Wang, S. C. Yan, P. J. Zhang, and Q. Wang, Phys. Rev. A **83**, 052707 (2011).

[60] R. H. Dalitz, Phys. Rev. **94**, 1046 (1954).

[61] R. H. Dalitz, Philos. Mag. **44**, 1068 (1953).

[62] J. Rajput, T. Severt, B. Berry, B. Jochim, P. Feizollah, B. Kaderiya, M. Zohrabi, U. Ablikim, F. Ziaee, K. Raju P., D. Rolles, A. Rudenko, K. D. Carnes, B. D. Esry, and I. Ben-Itzhak, Phys. Rev. Lett. **120**, 103001 (2018).

[63] K. Głuch, J. Fedor, S. Matt-Leubner, O. Echt, A. Stamatovic, M. Probst, P. Scheier, and T. D. Märk, J. Chem. Phys. **118**, 3090 (2003).

[64] H. J. Yang, E. Wang, W. X. Dong, M. Gong, Z. Shen, Y. Tang, X. Shan, and X. Chen, Phys. Rev. A **97**, 052703 (2018).

[65] S. Ohmura, K. Nagaya, F. Shimojo, and M. Yao, Z. Phys. Chem. **235**, 169 (2021).

[66] Z. Li, L. Inhester, C. Liekhus-Schmaltz, B. F. E. Curchod, J. W. Snyder, N. Medvedev, J. Cryan, T. Osipov, S. Pabst, O. Vendrell, P. Bucksbaum, and T. J. Martinez, Nat. Commun. **8**, 453 (2017).

[67] S. Maclot, D. G. Piekarski, A. Domaracka, A. Méry, V. Vizcaino, L. Adoui, F. Martín, M. Alcamí, B. A. Huber, P. Rousseau, and S. Díaz-Tendero, J. Phys. Chem. Lett. **4**, 3903 (2013).

[68] T. Jiang, B. Wang, Y. Zhang, L. Wei, S. Chen, W. Yu, Y. Zou, L. Chen, and B. Wei, Phys. Rev. A **100**, 022705 (2019).

[69] J. Yadav, C. P. Safvan, P. Bhatt, P. Kumari, J. Singh, and J. Rajput, J. Chem. Phys. **158**, 074302 (2023).

[70] Y. Gao, Y. Pan, S. Xu, K.-C. Lau, H. Yuan, Z. Yan, D. Guo, D. Zhao, X. Zhu, S. Yan, S. Zhang, Z. Xu, and X. Ma, Phys. Rev. A **107**, 012811 (2023).

[71] C. Ma, S. Xu, D. Zhao, D. Guo, S. Yan, W. Feng, X. Zhu, and X. Ma, Phys. Rev. A **101**, 052701 (2020).

[72] H. Yuan, S. Xu, E. Wang, J. Xu, Y. Gao, X. Zhu, D. Guo, B. Ma, D. Zhao, S. Zhang, S. Yan, R. Zhang, Y. Gao, Z. Xu, and X. Ma, J. Phys. Chem. Lett. **13**, 7594 (2022).

[73] C. C. Montanari and J. E. Miraglia, J. Phys. B: At. Mol. Opt. Phys. **49**, 175203 (2016).